J. Fluid Mech. (1987), *vol.* 180, *pp.* 343–369
Printed in Great Britain

A bifurcation study of laminar flow in a curved tube of rectangular cross-section

By KEITH H. WINTERS

Theoretical Physics Division, Harwell Laboratory, Didcot, Oxon OX11 0RA, UK

(Received 17 January 1985 and in revised form 21 December 1986)

The spiralling flow within a curved tube of rectangular cross-section normally forms two distinct cells in the plane of the cross-section, but a transition to a different, four-cell flow is known to occur at a critical value of the axial pressure gradient. This paper shows that, for a square cross-section, the transition is a result of a complex structure of multiple, symmetric and asymmetric solutions. The structure is revealed by solving extended systems of equations for steady-state, fully developed, laminar flow, in a finite-element approximation, to locate exactly the positions of singular points. Continuation methods are used to trace the paths of these points as the aspect ratio and radius of curvature vary. For a square cross-section, multiple, symmetric flows of both two and four cells are found in two distinct ranges of axial pressure gradient q. In addition, a pair of asymmetric solutions arise from a symmetry-breaking bifurcation point on the primary flow branch. The paths of limit points and symmetry-breaking bifurcation points are obtained as the aspect ratio γ varies, and a transcritical bifurcation point is found at $\gamma = 1.43$. For larger aspect ratios the secondary four-cell branch is disconnected from that of the primary two-cell flow. The bifurcation set in the two parameters q and γ has a complex structure, with a number of higher-order singularities; in particular, the path of limit points is found to cross in the manner of an unfolded swallowtail catastrophe. A stability analysis shows that all multiple solutions except the two-cell type are unstable with respect to either symmetric or antisymmetric perturbations. For values of the aspect ratio less than 1.43 there is a range of axial pressure gradients for which there is no stable flow. The critical Dean numbers of the singular points are found to vary strongly at small values of radius of curvature β, but the bifurcation set remains qualitatively the same. Previous work is interpreted in the light of the present results.

1. Introduction

The study of fluid flow within curved tubes has a long history, beginning with the observations of Thomson (1876); a summary of references to this early work is given by Manlapaz & Churchill (1980). Dean (1928) showed that the fully developed flow is characterized by a single parameter, a combination of the Reynolds number and the radius of curvature β of the coil, for large values of β. This parameter is now known as the Dean number, although several definitions of this quantity are in current use. We note that the flow in a curved tube is well approximated by a helical coil of small pitch (Manlapaz & Churchill 1980).

When fluid passes along a curved tube a centrifugal force induces a component of flow in the plane of the tube cross-section, resulting in a spiralling motion. When this secondary flow in the plane of the cross-section is represented by streamlines, then

typically there are two counter-rotating cells, disposed symmetrically about the radius of curvature of the coil.

In the early work the observed flow comprised two counter-rotating cells only. More recently, four-cell flows have been found, with the additional pair of cells adjacent to the outer wall of the tube. Joseph, Smith & Adler (1975), Cheng, Lin & Ou (1976), Ghia & Sokhey (1977) and De Vriend (1981) have predicted four-cell flows within rectangular cross-sections. The work of Masliyah (1980), Nandakumar & Masliyah (1982) and Dennis & Ng (1982) has revealed four-cell flows also, within circular and semicircular ducts. Experimental verification of these four-cell solutions is provided by Joseph *et al.* (1975) and Hille, Vehrenkamp & Schulz-DuBois (1985) for rectangular sections, and by Masliyah (1980) for semicircular sections.

In the case of circular and semicircular cross-sections, this recent work shows that the four-cell flows correspond to dual solutions of the governing equations, since they are found at the same Dean number as the two-cell flows, above a critical value. For rectangular cross-sections, however, the four-cell flow appears at a critical Dean number, as a transition from the two-cell flow, and no dual solutions have been reported.

Despite this work, our understanding of the four-cell flows is still very limited. It is unclear why they should appear as a transition from the normal flow, for rectangular cross-sections, but as dual solutions for circular and semicircular ducts. No computation has predicted more than two solutions of a particular flow, except for the preliminary work of Winters & Brindley (1984), yet an odd number of solutions is expected (Benjamin 1978) above the critical Dean number, with at least one solution being unstable. Moreover, where steady-state calculations have predicted a dual four-cell solution, there has been no indication as to its stability.

The aim of the present paper is to establish the precise solution structure that gives rise to the observed and predicted flows in curved tubes of rectangular cross-section. Since multiple solutions arise from the nonlinearities in the Navier–Stokes equations, the techniques of bifurcation theory are an appropriate tool for resolving this structure. In particular, so-called extended systems have been used successfully in a number of bifurcation studies involving ordinary differential equations. They have been applied recently to the study of bifurcations in the partial differential equations of fluid flow and heat transfer (Cliffe & Winters 1983; Cliffe 1983, 1984; Cliffe & Winters 1984, 1986; Winters & Cliffe 1985; Cliffe & Spence 1984; Winters & Brindley 1984; Winters, Cliffe & Jackson 1984; Cliffe & Mullin 1985). In this approach, the singular points of the equations that model the fluid flow are found by solving simultaneously the flow equations together with characteristic conditions that are satisfied specifically at the singular point. The solution of the extended system then converges to the solution of the basic equations at such a singular point, and reveals the exact location of the singularity. Continuation methods (Keller 1977) may then be applied to the extended system to follow the paths of singular points as other parameters in the problem vary.

Thus, the procedure adopted in this study may be summarized as follows:

(i) the basic Navier–Stokes equations for flow in a curved tube of square cross-section ($\gamma = 1$) are solved at increasing values of axial pressure gradient q, using continuation in q to follow the primary solution branch arising at $q = 0$. Limit points and symmetry-breaking bifurcation points are located approximately by monitoring the sign of the Jacobian determinant;

(ii) when a limit point or symmetry-breaking bifurcation point is found, the appropriate extended system based on the Navier–Stokes equations is solved to

locate exactly the position of the singular point on the solution branch. Then the paths of these singular points are obtained for rectangular cross-sections by continuation in the aspect ratio γ. This reveals secondary branches that are disconnected from the primary branch, and also higher-order singularities on the paths of singular points;

(iii) appropriate extended systems of Navier–Stokes equations are solved to locate exactly the higher-order singularities that arise on the paths of limit points and symmetry-breaking bifurcation points.

2. Theory

2.1. *Basic equations*

We consider laminar, steady, fully developed flow within a curved tube, and seek the steady-state solutions of the Navier–Stokes and continuity equations in the toroidal coordinate system (R, Y, Φ) shown in figure 1. In practice, it is more convenient to use the related coordinate system (X, Y, Z), where $X = R-C$, $\mathrm{d}Z = R\,\mathrm{d}\Phi$, and C is the radius of curvature, and the equations in these coordinates are non-dimensionalized using the following scales:

lengthscale A for the radial X- and axial Z-coordinates, where A is the half-width of the rectangular cross-section;

lengthscale B for the tangential Y-coordinate, where B is the half-height of the rectangular cross-section;

velocity scale ν/A, where ν is the kinematic viscosity;

pressure scale $\rho\nu^2/A^2$, where ρ is the density.

The above choice of a different scale for the Y-coordinate introduces the aspect ratio $\gamma = B/A$ as an explicit parameter in the equations, so that continuation in γ is possible.

With the above assumptions, the steady-state Navier–Stokes and continuity equations are

$$u\frac{\partial u}{\partial x}+\frac{v}{\gamma}\frac{\partial u}{\partial y}-\frac{w^2}{(x+\beta)}+\frac{\partial p}{\partial x}-\nabla^2 u+\frac{u}{(x+\beta)^2}=0, \tag{1}$$

$$u\frac{\partial v}{\partial x}+\frac{v}{\gamma}\frac{\partial v}{\partial y}+\frac{1}{\gamma}\frac{\partial p}{\partial y}-\nabla^2 v=0, \tag{2}$$

$$u\frac{\partial w}{\partial x}+\frac{v}{\gamma}\frac{\partial w}{\partial y}+\frac{uw}{(x+\beta)}+\frac{\beta}{(x+\beta)}q-\nabla^2 w+\frac{w}{(x+\beta)^2}=0, \tag{3}$$

and

$$\frac{1}{(x+\beta)}\frac{\partial}{\partial x}(x+\beta)\,u+\frac{1}{\gamma}\frac{\partial v}{\partial y}=0, \tag{4}$$

where

$$\nabla^2=\frac{1}{(x+\beta)}\frac{\partial}{\partial x}(x+\beta)\frac{\partial}{\partial x}+\frac{1}{\gamma^2}\frac{\partial^2}{\partial y^2}$$

and

$$q=\frac{\partial p}{\partial z}.$$

β is the non-dimensional radius of curvature C/A.

The boundary conditions are the usual Dirichlet no-slip and pressure-reference conditions:

$u = v = w = 0$ on the wall of the pipe;

$p = 0$ at an interior point.

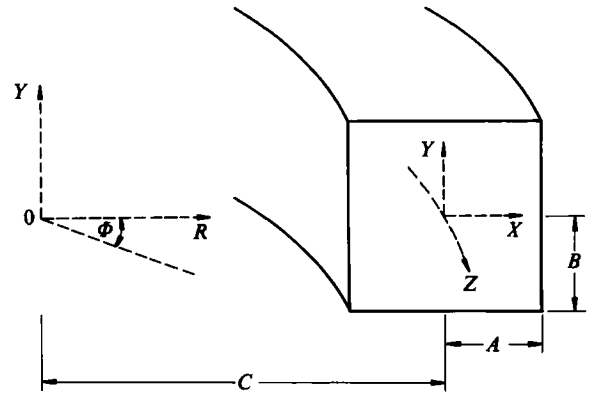

FIGURE 1. Geometry for a curved tube of rectangular cross-section.

The stream function S was obtained from the computed velocity components, as an aid to visualizing the secondary flow. We use the definition

$$u = \frac{\beta}{(x+\beta)\gamma}\frac{\partial S}{\partial y}; \quad v = -\frac{\beta}{(x+\beta)}\frac{\partial S}{\partial x};$$

so that S is given by

$$\frac{(x+\beta)}{\beta}\left(\frac{\partial v}{\partial x}-\frac{1}{\gamma}\frac{\partial u}{\partial y}\right)-\frac{2}{(x+\beta)}\frac{\partial S}{\partial x}+\nabla^2 S = 0,$$

where ∇^2 is defined in the equation following (4).

For a given cross-section, the Navier–Stokes equations contain two parameters, the axial pressure gradient q and radius of curvature β, which determine the flow. Dean (1928) showed that, for large enough radii of curvature, q and β can be combined into a single parameter that characterizes the flow, the Dean number Dn. The results of the present work are obtained explicitly at various values of β, to establish to what extent the approximation of Dean is valid.

We define the Dean number Dn as the following combination of Reynolds number Re and the radius of curvature β:

$$Dn = Re\,\beta^{-\frac{1}{2}} = \frac{D}{A}\overline{w}\beta^{-\frac{1}{2}}.$$

The Reynolds number (based on the non-dimensional mean axial velocity $\overline{w}$ and hydraulic diameter D) is defined as

$$Re = \frac{D\overline{w}}{A}.$$

The mean axial velocity $\overline{w}$ is calculated from

$$\overline{w} = \frac{\int w(x,y)\,(x+\beta)\,\mathrm{d}x\,\mathrm{d}y}{\int (x+\beta)\,\mathrm{d}x\,\mathrm{d}y}.$$

The hydraulic diameter is defined as four times the ratio of the cross-sectional area to the perimeter, and has the following value for the rectangular cross-section considered here:

$$D = \frac{4AB}{A+B} = \frac{4A\gamma}{1+\gamma}.$$

Various definitions of the Dean number are widely used, based on either the axial pressure gradient or the mean axial velocity, together with other obvious differences arising from the choice of lengthscale. The definition of the Reynolds number is usually based on the mean axial velocity, but sometimes the axial pressure gradient is used. We stress that the Dean number derived in the present work uses a Reynolds number based on mean axial velocity and hydraulic diameter, and a radius of curvature based on half-width.

2.2. *The finite-element formulation*

A weak formulation of the equations was derived by multiplying each equation by a test function and integrating the second-order terms by parts, to give

$$\int t_1\left(u\frac{\partial u}{\partial x}+\frac{v}{\gamma}\frac{\partial u}{\partial y}-\frac{w^2}{(x+\beta)}+\frac{\partial p}{\partial x}+\frac{u}{(x+\beta)^2}-\frac{1}{(x+\beta)}\frac{\partial u}{\partial x}\right)\mathrm{d}x\,\mathrm{d}y + \int\left(\frac{\partial t_1}{\partial x}\frac{\partial u}{\partial x}+\frac{1}{\gamma^2}\frac{\partial t_1}{\partial y}\frac{\partial u}{\partial y}\right)\mathrm{d}x\,\mathrm{d}y = 0, \quad (5)$$

$$\int t_1\left(u\frac{\partial v}{\partial x}+\frac{v}{\gamma}\frac{\partial v}{\partial y}+\frac{1}{\gamma}\frac{\partial p}{\partial y}-\frac{1}{(x+\beta)}\frac{\partial v}{\partial x}\right)\mathrm{d}x\,\mathrm{d}y+\int\left(\frac{\partial t_1}{\partial x}\frac{\partial v}{\partial x}+\frac{1}{\gamma^2}\frac{\partial t_1}{\partial y}\frac{\partial v}{\partial y}\right)\mathrm{d}x\,\mathrm{d}y = 0, \quad (6)$$

$$\int t_1\left(u\frac{\partial w}{\partial x}+\frac{v}{\gamma}\frac{\partial w}{\partial y}+\frac{uw}{(x+\beta)}+\frac{\beta}{(x+\beta)}q+\frac{w}{(x+\beta)^2}-\frac{1}{(x+\beta)}\frac{\partial w}{\partial x}\right)\mathrm{d}x\,\mathrm{d}y + \int\left(\frac{\partial t_1}{\partial x}\frac{\partial w}{\partial x}+\frac{1}{\gamma^2}\frac{\partial t_1}{\partial y}\frac{\partial w}{\partial y}\right)\mathrm{d}x\,\mathrm{d}y = 0, \quad (7)$$

$$\int t_2\left(\frac{\partial u}{\partial x}+\frac{u}{(x+\beta)}+\frac{1}{\gamma}\frac{\partial v}{\partial y}\right)\mathrm{d}x\,\mathrm{d}y = 0. \quad (8)$$

The test functions t_1 and t_2 have square-integrable first derivatives and t_1 vanishes on the boundary of the tube.

In the finite-element approximation to these weak equations, the velocity components and pressure are approximated by expansions in quadratic and linear basis functions respectively. Similarly, the test functions t_1 and t_2 are chosen from the set of quadratic and linear basis functions respectively. Six-noded triangular elements were used, with the quadratic basis functions defined at all nodes and the linear functions defined at the vertex nodes only.

2.3. *Extended systems*

Let the discrete equations that result from the finite-element approximation of the Navier–Stokes equations be written

$$f(\chi, \lambda) = 0, \quad (9)$$

where χ is the solution vector and λ is the vector of parameters for the problem, $\lambda = (q, \gamma, \beta)$. To find singular points of codimension 1, (9) is solved for fixed aspect ratio γ and radius of curvature β to obtain the critical value of axial pressure gradient q at which the solution χ is singular. For singular points of codimension 2 only the radius of curvature β is fixed, and (9) is solved to obtain the critical values of the axial pressure gradient q and aspect ratio γ at which the solution χ is singular.

A singular point of the set of equations (9) may be found by solving them simultaneously with conditions that are satisfied at that point. The solution of such

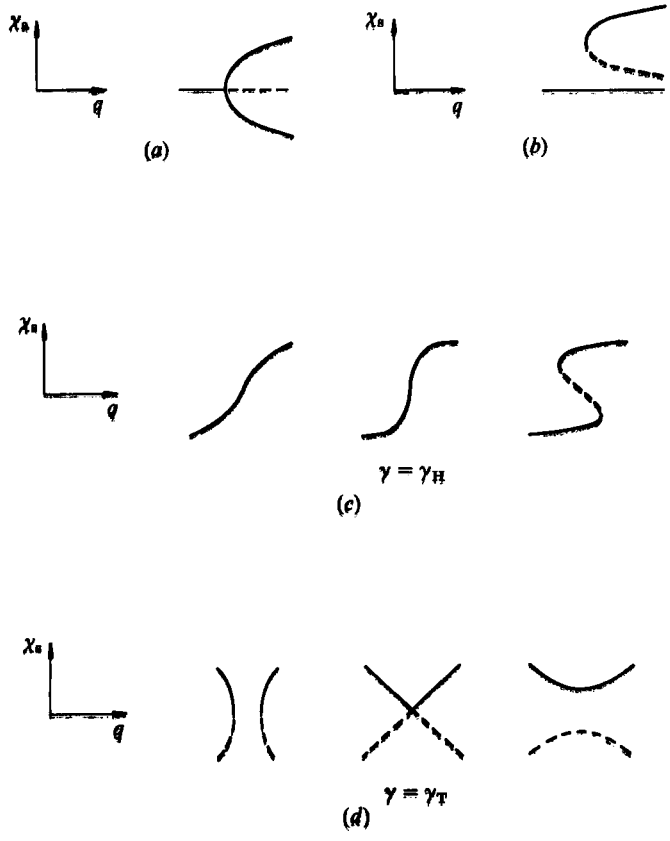

FIGURE 2*a–d*. For caption see facing page.

an extended system then locates explicitly the singular point, as well as the solution χ of the basic equations. The extended systems in the present study were all solved by Newton's method, which converges quadratically provided the initial guesses for λ and χ are sufficiently good. The precise form of extended system depends on the type of singular point, and alternative forms are discussed in the following sections. The present problem actually exhibits all possible singular points of codimension 1 and 2. These are represented schematically in figure 2 as state diagrams, where a symmetric or antisymmetric measure of the solution is drawn as a function of the axial pressure gradient q. Wherever a broken line replaces a solid line in these figures, there is a change either from a stable to an unstable solution or vice versa.

2.3.1. *Symmetry-breaking bifurcation points*

A symmetry-breaking bifurcation point is represented in figure 2(*a*). As the parameter q increases, there is a pitchfork bifurcation into three branches, and the upper and lower branches correspond to asymmetric solutions. Symmetry-breaking bifurcation points in the present problem were located with the algorithm of Werner & Spence (1984), which proposes the extended set of equations

$$\left.\begin{aligned} f(\chi, \lambda) &= 0, \\ f_\chi(\chi, \lambda)\,\phi &= 0, \\ l(\phi) &= 1. \end{aligned}\right\} \tag{10}$$

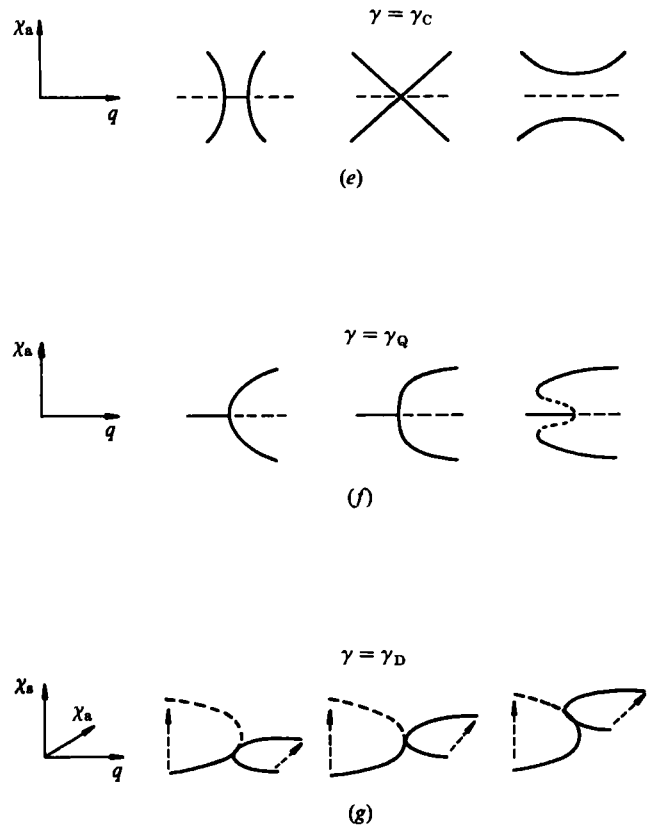

FIGURE 2. State diagrams for singular points of codimension 1 and 2: (*a*) symmetry-breaking bifurcation point; (*b*) limit point; (*c*) non-degenerate hysteresis point; (*d*) transcritical bifurcation point; (*e*) coalescence point; (*f*) quartic point; (*g*) double-singular point.

Here, $\boldsymbol{\phi}$ is the right eigenvector of the Jacobian matrix, and $\boldsymbol{l}$ is a linear functional which normalizes $\boldsymbol{\phi}$. The solution $\boldsymbol{\chi}$ and the eigenvector $\boldsymbol{\phi}$ must belong to the subspace of symmetric and antisymmetric flows respectively. The algorithm is applied to the subdomain over which the symmetry of the solution is broken. In the present case, the equations were solved in the upper half of the cross-section.

Details of the finite-element formulation of this algorithm are to be found in Cliffe & Winters (1986).

2.3.2. *Limit points*

A limit point, or one-sided bifurcation point, occurs when two additional solutions become possible above a critical value of q. This is illustrated in figure 2(*b*). The alternative configuration with two secondary modes disappearing above a critical q is not shown. Limit points were found using an algorithm due to Moore & Spence (1980). The extended set of equations is

$$\left.\begin{aligned} \boldsymbol{f}(\boldsymbol{\chi}, \lambda) &= 0, \\ \boldsymbol{f}_{\boldsymbol{\chi}}(\boldsymbol{\chi}, \lambda)\,\boldsymbol{\phi} &= 0, \\ \boldsymbol{l}(\boldsymbol{\phi}) &= 1. \end{aligned}\right\} \tag{11}$$

In this case, unlike the previous algorithm, the solution and eigenvector are not constrained to symmetric and antisymmetric subspaces.

The Moore–Spence algorithm has been used in a finite-element formulation by Cliffe (1983, 1984), Cliffe & Winters (1984), Winters & Brindley (1984) and Cliffe & Mullin (1985).

2.3.3. *Non-degenerate hysteresis points*

A non-degenerate hysteresis point occurs as a second parameter γ varies through a critical value γ_H, and a pair of limit points either appear or disappear, as shown in figure 2(*c*). The paths of limit points then meet at a cusp point in the two-parameter space (q, γ). Non-degenerate hysteresis points were located using an extended system similar to that of Roose & Caluwaerts (1984). The equations (11) are solved with the additional condition

$$\boldsymbol{\psi} \boldsymbol{f}_{\chi\chi}(\chi, \lambda)\, \boldsymbol{\phi}\boldsymbol{\phi} = 0, \tag{12}$$

where $\boldsymbol{\psi}$ is the left eigenvector of the Jacobian matrix. This condition has been used by Spence & Jepson (1984) (see also Jepson & Spence 1984, 1985).

2.3.4. *Transcritical bifurcation points*

A transcritical bifurcation point occurs at a critical value of the second parameter γ_T, when two limit points merge as in figure 2(*d*). It corresponds to a turning-point on the path of limit points in the two-parameter space (q, γ). The transcritical bifurcation point of figure 2(*d*) was found by solving (11) with the additional condition (Jepson & Spence 1984)

$$\boldsymbol{\psi} \boldsymbol{f}_q(\chi, \lambda) = 0. \tag{13}$$

This has been used in a finite-element formulation by Cliffe (1984).

2.3.5. *Coalescence points*

The state diagram for a coalescence point is similar to that of the previous singular point, and corresponds to the merging of two symmetry-breaking bifurcation points at a critical value γ_C, as in figure 2(*e*). It appears as a turning-point on the path of symmetry-breaking bifurcation points in the space (q, γ). The coalescence point of figure 2(*e*) was located by solving (10) with the additional condition (Cliffe & Spence 1984)

$$\boldsymbol{\psi}(\boldsymbol{f}_{q\chi}(\chi, \lambda)\, \boldsymbol{\phi} + \boldsymbol{f}_{\chi\chi}(\chi, \lambda)\, \boldsymbol{\phi}\boldsymbol{h}_q) = 0, \tag{14}$$

where

$$\boldsymbol{f}_\chi(\chi, \lambda)\, \boldsymbol{h}_q + \boldsymbol{f}_q = 0,$$

and $\boldsymbol{h}_q$ belongs to the subspace of symmetric flows.

2.3.6. *Quartic points*

A quartic point occurs at the transition between a supercritical and a subcritical symmetry-breaking bifurcation, as illustrated in figure 2(*f*). At the critical value of the second parameter γ_Q, the asymmetric branch has a quartic dependence on the difference of q and its critical value. This contrasts with the usual quadratic dependence of supercritical and subcritical bifurcations. In the two-parameter space (q, γ), the quartic point marks the emergence of a path of limit points from the path

of symmetry-breaking bifurcation points. Quartic points were located by solving (10) with the additional condition (Cliffe & Spence 1984)

$$\psi(f_{\chi\chi\chi}(\chi,\lambda)\,\phi\phi\phi+3f_{\chi\chi}(\chi,\lambda)\,\phi g)=0, \tag{15}$$

where

$$f_\chi(\chi,\lambda)\,g+f_{\chi\chi}(\chi,\lambda)\,\phi\phi=0.$$

and g belongs to the subspace of symmetric flows.

2.3.7. *Double-singular point*

A double-singular point occurs at a critical value γ_{D} when a symmetry-breaking bifurcation point passes around a limit point, as illustrated in figure 2(*g*). In the two-parameter space (q,γ), the paths of limit points and symmetry-breaking bifurcation points touch but do not cross. A path of Hopf bifurcation points arises at a double-singular point but these were not computed in the present study.

Double-singular points were located by solving the set of equations (Werner 1984)

$$\left.\begin{aligned} f(\chi,\lambda)&=0,\\ f_\chi(\chi,\lambda)\,\phi_{\mathrm{s}}&=0,\\ f_\chi(\chi,\lambda)\,\phi_{\mathrm{a}}&=0,\\ l_{\mathrm{s}}(\phi_{\mathrm{s}})&=1,\\ l_{\mathrm{a}}(\phi_{\mathrm{a}})&=1, \end{aligned}\right\} \tag{16}$$

where ϕ_{s} and ϕ_{a} belong to the subspaces of symmetric and antisymmetric flows respectively.

2.3.8. *Continuation*

The present problem involves three parameters and we wish to study the behaviour of the flow as each of these is changed. It is clearly essential to have an efficient method for computing the solution as these parameters vary; Euler–Newton continuation is an effective means of following a particular solution branch. In its most simple form the solution χ^0 obtained at $q=q^0$, and its derivative $\partial\chi^0/\partial q$, are used to predict the solution χ^1 at a new value q^1, from

$$\chi^1=\chi^0+\frac{\partial\chi^0}{\partial q}(q^1-q^0).$$

The Newton–Raphson iterations converge rapidly at each value of q, for a suitable step size (q^1-q^0), but this procedure ultimately fails at a limit point in the solution curve, where the Jacobian matrix of (9) is singular. A better method uses a pseudoarclength parameter s to parametrize the solution (Keller 1977). As an example, we suppose that continuation in q is required. Instead of the basic Navier–Stokes equations, we solve the extended system

$$\left.\begin{aligned} f(\chi,\lambda)&=0,\\ N(\chi,q,s)&=0, \end{aligned}\right\} \tag{17}$$

where

$$N=\left[\frac{\partial\chi}{\partial s}(s_0)\right]^{\mathrm{T}}[\chi(s)-\chi(s_0)]+\frac{\partial q}{\partial s}(s_0)[q(s)-q(s_0)]-(s-s_0).$$

With Euler–Newton continuation in s rather than q, it is possible to follow the solution around a limit point, since the Jacobian matrix of system (17) is non-singular.

The presence of a symmetry-breaking bifurcation point or limit point is determined by monitoring the Jacobian determinant, which changes sign as the singular point is passed.

Continuation of the solution onto the asymmetric branch which arises from a symmetry-breaking bifurcation point was achieved by using the eigenvector at the singular point as a guess for the derivative $\partial\chi^0/\partial q$ of the asymmetric solution.

The paths of singular points were traced out by applying continuation in γ and β to the appropriate extended system, augmented in the manner of (17).

The Keller pseudoarclength method was found to be very effective in determining the complex structure of the bifurcation set of the present problem. A refinement would be to use an algorithm for automatically changing the step length, as in Jackson & Winters (1984), but no such procedure was adopted here. Instead, the step size was simply increased by a constant factor of 1.4 each time the iterations converged successfully, and halved otherwise.

3. Results

Since we are interested in possible asymmetric flows, the equations were solved initially on a grid of elements over the full cross-section, rather than the usual half-grid with imposed symmetry about the horizontal mid-plane. A grid consisting of n and m elements in the x- and y-directions respectively will be denoted an $n \times m$ grid, and the letter h or f will be appended to indicate that either the half- or full cross-section was discretized by those elements. We obtained most of the initial solutions on a 14×14f grid to give an approximation to the solution structure, and then we refined the grid to find the precise location of limit points and bifurcation points. An interesting phenomenon was the appearance of spurious symmetry-breaking bifurcation points on a grid that was too coarse. For example, a 6×6f grid was found to give rise to three such points over a small range of q, which vanished on refining the grid to 14×14 elements.

Once a symmetry-breaking bifurcation point or limit point was found on the full grid, then its position was located more accurately on a half-grid using the appropriate extended system. Similarly, the paths of the singular points and the positions of higher-order singularities were obtained on a half-grid.

All computations were carried out using the ENTWIFE code, developed at Harwell for solving problems of heat transfer and fluid flow, and based on the TGSL library of finite-element subroutines. In all calculations the convergence criterion used for terminating the Newton–Raphson iterations was that the difference in absolute value of each of the global freedoms (including the bifurcation parameters) between successive iterations was less than 10^{-5}. At this threshold the iterations are terminated well within the region of quadratic convergence.

3.1. *Square cross-section*

We consider first a square cross-section, $\gamma = 1$, and a fixed radius of curvature of $\beta = 50$. Results were obtained for a small axial pressure gradient q, by continuation from an initial guess with zero q.

3.1.1. *Solution structure*

The solution structure found for $\gamma = 1$ and $\beta = 50$ is complex and it is best discussed with reference to the schematic diagram of figure 3. This records the variation of some measure of the symmetric solution χ_s, the central axial velocity

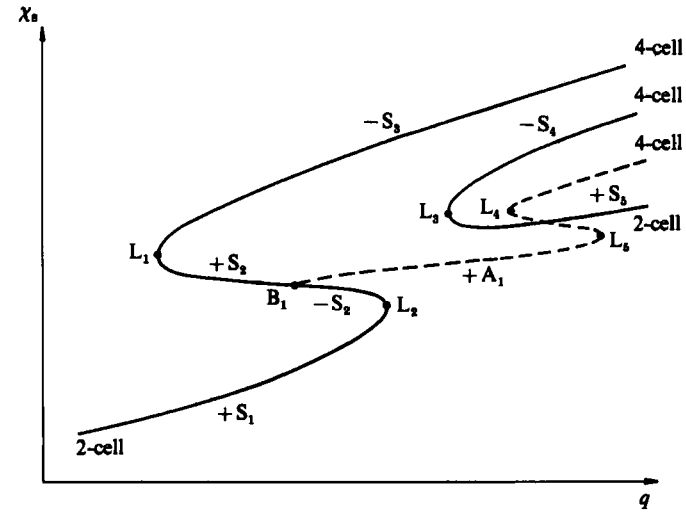

FIGURE 3. Schematic state diagram showing the variation of a measure of the symmetric component of the solution χ_s with the axial pressure gradient q, for a square cross-section. S denotes a symmetric solution, A an asymmetric solution, B a symmetry-breaking bifurcation point and L a limit point. The sign of each branch is $(-1)^n$, where n is the number of negative eigenvalues of the Jacobian matrix. A broken line indicates an asymmetric solution.

for example, with axial pressure gradient q. The branches that correspond to symmetric and asymmetric solutions are shown as solid and broken lines respectively. The structure of the symmetric solutions is that of an unfolded transcritical bifurcation with an additional limit point. The branch S_1 develops continuously from the origin into the branch S_3, through limit points L_2 and L_1. A disconnected branch with a limit point at L_3 lies at higher values of q. The curves labelled S_1 and S_5 are of symmetric two-cell type, away from the limit points, while those labelled S_2, S_3 and S_4 correspond to four cells away from the limit points.

A pair of asymmetric solutions A_1 arise from a symmetry-breaking bifurcation point B_1 on the branch S_2. This pair, which have identical symmetric components, appear as one branch on the present figure. If one imagines a measure of the antisymmetric component of the solution along an axis out of the page, then one asymmetric branch emerges from B_1 out of the page, and the other goes into the page; A_1 is the projection of this pair of solutions onto the page. The asymmetric branch itself has a pair of limit points, L_4 and L_5, and it will be seen later that they arise at two quartic points which occur at higher aspect ratio.

It should be stressed that the symmetry-breaking bifurcation point appears only when the problem has *exact* symmetry about the horizontal axis. Any asymmetry in the problem unfolds the bifurcation point, so that one of the asymmetric solutions develops smoothly from the $+S_2$ branch, while the other develops from the $-S_2$ branch, both without bifurcation. This effect was demonstrated by using a grid with an asymmetric pattern of elements. The unfolding will be present to some extent in any experiment, especially when the curved tube is approximated by a helical coil of small pitch, and the amount of unfolding will depend on the degree of asymmetry. We note that this unfolding alone cannot stabilize the asymmetric branch.

The actual solution structure for $\gamma = 1$ and $\beta = 50$, predicted on a 14×14f grid, is shown in figure 4(a) using the central axial velocity as a measure of the solution.

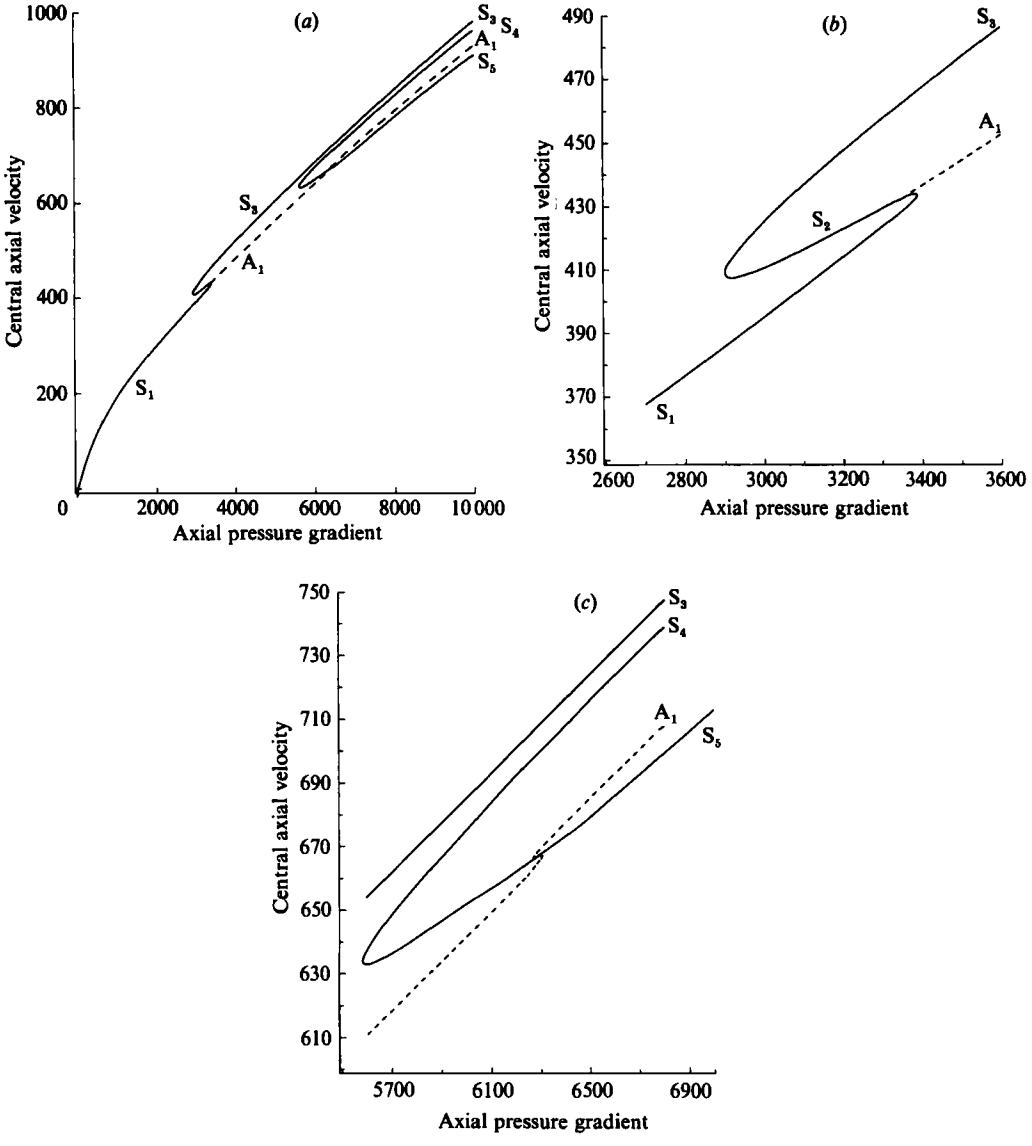

FIGURE 4. (*a*) Computed state diagram showing the variation of central axial velocity with q, for a square cross-section with radius of curvature $\beta = 50$. (*b*) Enlargement in region of lowest two limit points. (*c*) Enlargement in region of highest three limit points.

Figure 4(*b*, *c*) shows enlargements of this in the region of the limit points. The closeness of the different solutions is interesting, and the values of the central axial velocity for a given q generally lie within 10% of one another. Also, the symmetry-breaking bifurcation point B_1 lies very close to the limit point L_2, and these features caused some difficulty in obtaining the solution structure. Initially, the primary branch S_1 was followed by continuation in q, but beyond $q = 3400$ the flow was found to change to a four-cell type with a slight asymmetry; the solution had been continued from S_1 to A_1. After $q = 5600$ a transition back to two-cell flow was found. It was only by forcing very small steps in the pseudoarclength parameter s that we were able to follow the primary branch continuously from S_1 on to S_2.

Singular point	Grid	q	Dn
L_1	20 × 20h	2896.24	80.15
	16 × 16h	2897.64	80.18
	12 × 12h	2904.35	80.35
L_2	20 × 20h	3416.32	92.72
	16 × 16h	3416.78	92.73
	12 × 12h	3413.27	92.64
L_3	20 × 20h	5564.17	134.9
	16 × 16h	5574.21	135.1
	12 × 12h	5616.85	136.1
B_1	20 × 20h	3371.07	91.72
	16 × 16h	3371.68	91.74
	12 × 12h	3369.95	91.70

TABLE 1. Singular points of codimension 1, at $\gamma = 1$ and $\beta = 50$: L, limit point; B, symmetry-breaking bifurcation point

The values of the limit and symmetry-breaking bifurcation points labelled L_1, L_2, L_3 and B_1 on figure 3 are given in table 1. They are tabulated for the finest grid considered and also for coarser grids to give some indication of the degree of grid convergence. The error in the singular points is expected to vary as the fourth power of the mesh spacing, a rate of convergence equal to the square of the rate of convergence of the velocity components (Winters & Cliffe 1985).

The nature of the flow on each of the branches was established by computing the stream function. Well-defined two- or four-cell flows were found, except near the limit points, where the flow was of intermediate type. Figure 5 compares contour plots of stream function and axial velocity for the one asymmetric and three symmetric solutions at $q = 3390$. This value of q is just less than the critical value at the limit point L_2. The figures show that the flow on the S_1 and S_2 branches is similar and weakly of the four-cell type. On the other hand, the secondary pair of cells in the four-cell flow on the S_3 branch are strong. Only one of the pair of asymmetric solutions is shown and the other is obtained by reflection about the horizontal mid-plane. Although the secondary vortex pair is weak the asymmetry is clear.

Before comparing the flows with the results of previous work it is important to discuss the stability of each of the branches, and this is done in the following section.

3.1.2. *Stability of flows*

A solution of (9) is stable when the Jacobian matrix has no negative eigenvalues. We obtain an indication of the stability from the sign of the Jacobian determinant, which is equal to $(-1)^n$, where n is the number of negative eigenvalues of the matrix. Thus, a negative value of the Jacobian determinant implies that the corresponding flow is unstable, but a positive value is insufficient to indicate stability.

The sign of the Jacobian determinant for each of the branches in the present case is given on figure 3, which shows that the four-cell flows on S_3 and S_4 are unstable. The S_1 branch has a positive Jacobian determinant, and the corresponding two-cell flow must be stable, since the branch connects smoothly with the origin of the state diagram at $q = 0$, and has no bifurcation points. The Jacobian determinant for the two-cell flow on S_5 is also positive, and we expect the flow to be stable, since this

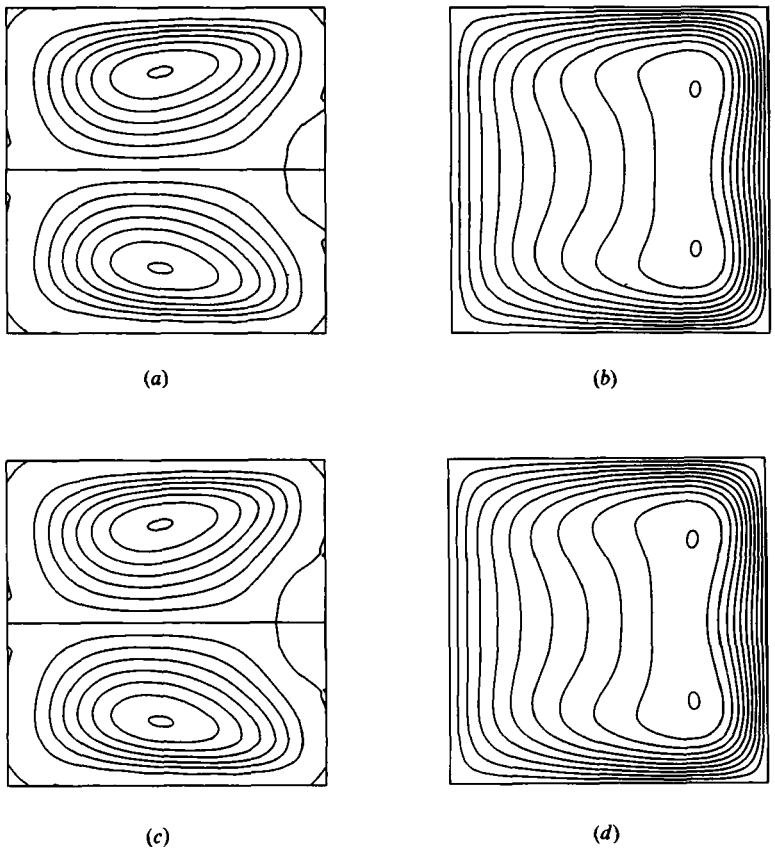

FIGURE 5*a–d*. For caption see facing page.

branch is continuous with S_1 for an appropriate value of the parameter that unfolds the transcritical bifurcation. As for the remaining branches, their stability can be inferred as follows. There are no negative eigenvalues on S_1, but as we pass around the limit point L_2, on to S_2, then one real eigenvalue corresponding to a symmetric eigenvector becomes negative, and so does the Jacobian determinant. As q is decreased, we pass through the symmetry-breaking bifurcation point B_1 on S_2 and a second eigenvalue becomes negative, this time corresponding to an antisymmetric eigenvector. The Jacobian determinant is now positive again but the flow is unstable. As we vary q further we pass around the limit point L_1 onto the curve S_3 and the negative eigenvalue corresponding to the symmetric eigenvector becomes positive. There remains one negative eigenvalue and the Jacobian determinant is negative. Thus the four-cell flow on S_3 is unstable to perturbations that break the horizontal symmetry. The asymmetric branch A_1 has the same stability properties as the $+S_2$ branch, and has two negative eigenvalues making it unstable.

We can summarize the above discussion by stating that all the solutions are unstable, except those on the two-cell branches S_1 and S_5, when perturbations that break the horizontal symmetry are taken into account. This has important implications for calculations that impose symmetry over the half-domain. Then the asymmetric branch A_1 vanishes and the four-cell branch is predicted to be stable. Our analysis also shows that for square cross-sections there is a range of q for which

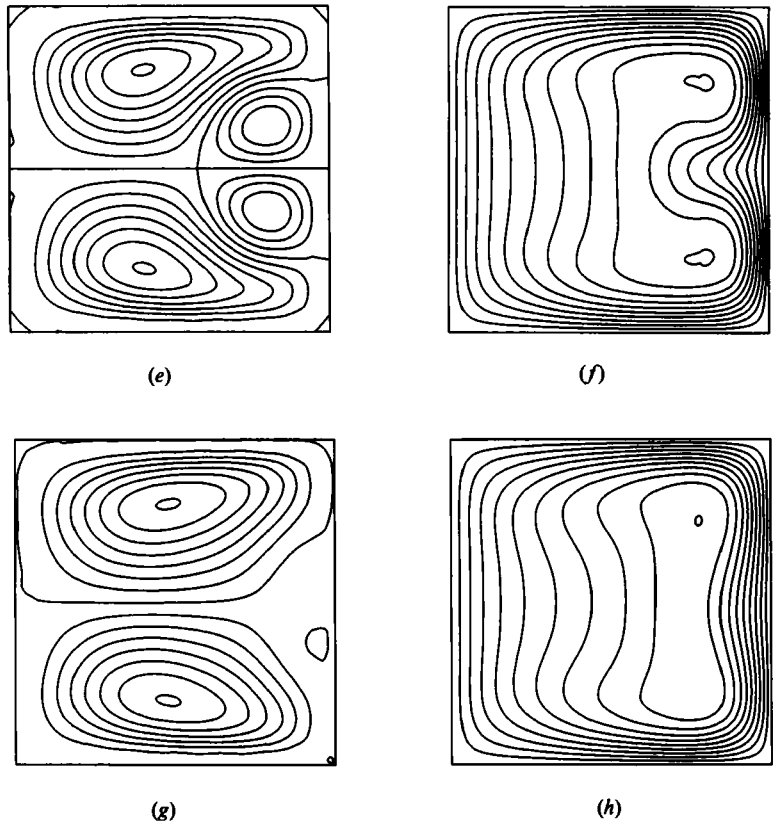

FIGURE 5. Multiple solutions for the square cross-section at an axial pressure gradient $q = 3390$ and radius of curvature $\beta = 50$. (*a*) Streamlines and (*b*) axial velocity contours on the branch S_1; (*c*) streamlines and (*d*) axial velocity contours on the branch S_2; (*e*) streamlines and (*f*) axial velocity contours on the branch S_3; (*g*) streamlines and (*h*) axial velocity contours on the branch A_1.

there are no stable solutions. We note that our assumption of fully developed flow limits our analysis to disturbances that preserve the translational $Z-$symmetry, and there may be further bifurcations to flows that break this symmetry and that cannot be found in the present treatment.

3.1.3. *Comparison with previous work*

We are now able to interpret the results of previous work according to the solution structure that we have found. The four-cell flows, which have been predicted previously for square cross-sections, appear as a transition from the two-cell flow at a given Dean number. Theoretical work has shown this transition to occur at:

Dn between 95 and 107 for a radius of curvature $\beta = 100$ (Joseph *et al.* 1975);

$Dn = 101$ for $\beta = 71$ (Ghia & Sokhey 1977);

Dn between 95 and 108 for $\beta = 10$ (De Vriend 1981);

Dn between 107 and 143 for $\beta = 200$ (Cheng *et al.* 1976).

The transition is clearly associated with the limit point L_2 of figures 3 and 4, since the two-cell flow ceases to exist at that point, and reappears only at the limit point L_3. The calculations of Joseph *et al.*, De Vriend and Cheng *et al.* were carried out on a half-grid with imposed symmetry about the horizontal centreline. As discussed, this

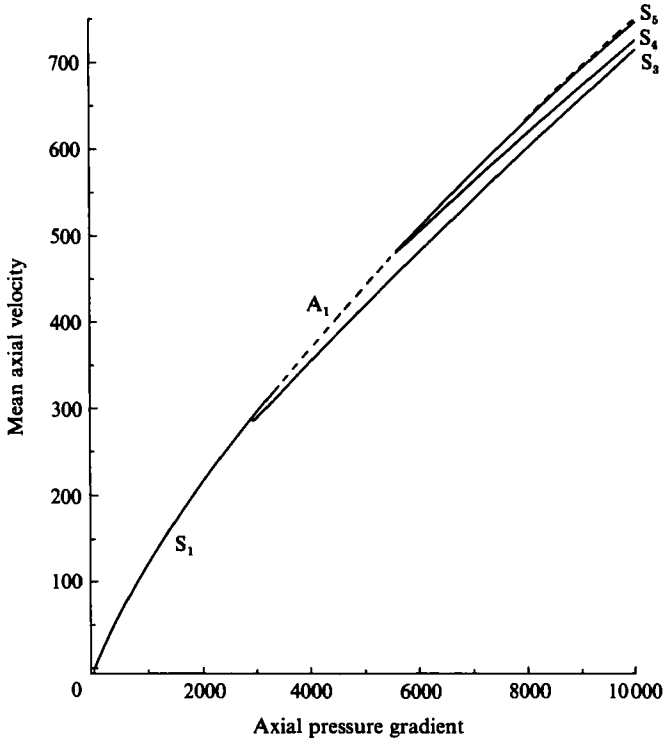

FIGURE 6. The variation of mean axial velocity $\overline{w}$ with axial pressure gradient q, for a square cross-section with radius of curvature $\beta = 50$. In this case the Dean number is $Dn = 0.283\overline{w}$.

does not permit asymmetric solutions and removes the asymmetric branch A_1 of figure 3. Thus, in these three calculations the predicted four-cell flow corresponds to a transition from the S_1 to the S_3 branch at the critical value of q associated with the limit point L_2. It is interesting to note that the authors would have observed a hysteresis effect had they *decreased* the axial pressure gradient q, on obtaining a four-cell flow. We have also shown that the S_3 branch is stable when symmetry is imposed, and this agrees with the fact that Joseph *et al.* were able to predict the four-cell flow with a transient method. Regarding the work of Ghia & Sokhey, they give computational times for both a full and a half-grid, and it is unclear which was used to predict their four-cell flow. However, the secondary pair of cells in their four-cell flow is comparable in strength with the primary cells. This would indicate that it corresponds to the branch S_3, as in the previous calculations.

In table 1 we give the values of the Dean numbers corresponding to the critical values of q for the singular points of figure 3. The critical Dean number for the L_2 limit point is predicted as 92.7, which is lower than the transitional values found in the other work. However, it should be stressed that the Dean number is *not* an independent parameter of the calculation. It is calculated from the mean axial velocity, which is a non-unique function of q. Figure 6 shows the variation of the mean axial velocity $\overline{w}$ with q, for $\gamma = 1$ and $\beta = 50$. In this case the Dean number is given by $Dn = 0.283\overline{w}$. It is clear that the Dean number at the critical value of q for the limit point L_2 is different on the two- and four-cell branches. The Dean number for the appearance of the four-cell flow at L_2 is 89.1 compared with a Dean number of

92.7 for the disappearance of the two-cell flow. It is also apparent that the Dean number is *decreasing* as the limit point L_2 is approached along the S_1 branch, so that the critical Dean number is less than the maximum attained, although this effect seems to be small in the present case. It should be noted also that the values of the radius of curvature adopted in the various calculations vary widely. The effect of this is considered in §3.3.

The experimental work with square cross-sections also indicates a transition from two- to four-cell flow, as in the calculations. Experimental work has shown this transition to occur at:

Dn of around 100 for a radius of curvature $\beta = 7.7$ (Joseph *et al.* 1975);

$Dn = 106$ for $\beta = 12.9$ (Hille *et al.* 1985).

The observation of a four-cell flow appears to conflict with the structure predicted in figure 3, which shows that only the two-cell flow is stable, and that there are no stable flows for values of q between 3413 and 5617, corresponding to Dean numbers of 92.6 and 136.1. Unfortunately, the experiments of Joseph *et al.* (1975) were, in their own words, insufficiently quantitative to check the details of the flow. They describe only a swirling pattern near the outer face, in addition to the primary cells. On the other hand, the experiments of Hille *et al.* (1985) are very detailed, but the flow in their work is not fully developed. However, a striking feature of the work of Hille *et al.* is the distinct asymmetry shown in their visualization of the four-cell flow, as found for the predicted flow on branch A_1 of figure 3. The identification of their four-cell flow with the A_1 branch is given further support by their measurement of the strength of the secondary vortex pair. They find that it increases from zero at the transition, reaches a maximum, then decreases until the four-cell flow changes back to two-cells. This behaviour is not characteristic of the four-cell flow on the S_3 branch, as is clear from figure 5, since the secondary vortex pair is already very strong at the transitional value of q.

Thus, we interpret the observed transition to four-cell flow as the transition from the symmetric branch S_1 to the asymmetric branch A_1. This still leaves the question of the predicted instability of the branch A_1. One possible mechanism which could stabilize the flow on the asymmetric branch is the presence of a Hopf bifurcation point on A_1. A Hopf bifurcation occurs when a complex pair of eigenvalues passes between the positive and negative real half-planes, and causes a transition to time-periodic flow. This bifurcation is difficult to detect in a steady calculation, since there is no change in sign of the Jacobian determinant. If there were such a bifurcation on the A_1 branch, corresponding to the two negative eigenvalues on A_1 becoming positive, then a time-periodic *unstable* solution would bifurcate from the singular point, stabilizing the asymmetric branch at higher q.

In order to investigate this possible mechanism, we carried out an eigenvalue analysis on the A_1 branch, as follows. We introduced the time-dependent terms in the Navier–Stokes equations (1)–(3) and assumed a time-dependence $e^{-\sigma t}$. Incorporating these terms in (5)–(7) leads to an eigenvalue problem of the form

$$\boldsymbol{f}_x X = \sigma \boldsymbol{M} X,$$

where $\boldsymbol{f}_x$ is the Jacobian matrix and $\boldsymbol{M}$ is the mass matrix arising from the time-dependent terms of the Navier–Stokes equations. This equation was solved for the lowest 20 eigenvalues σ at selected values of q on the A_1 branch. At $q = 3348$, just higher than the symmetry-breaking bifurcation point B_1, two negative real eigenvalues were found. At $q = 3390$, just below the transitional value L_2, these had collided and formed a complex pair of negative real part, with imaginary part equal

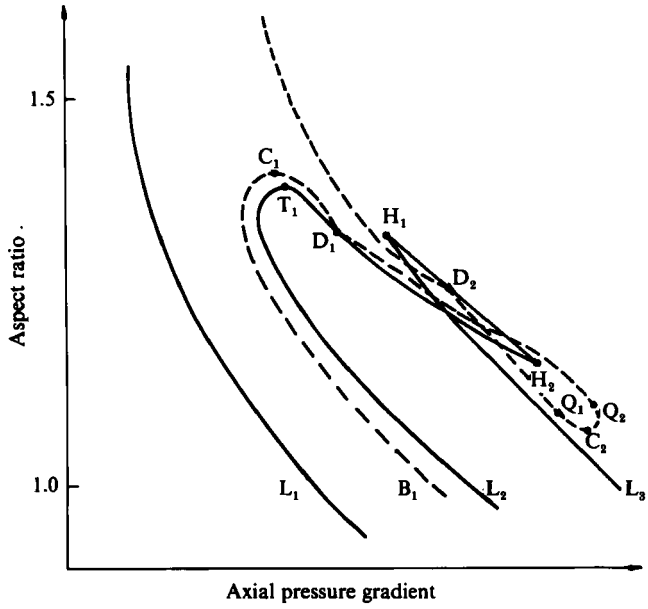

FIGURE 7. Schematic diagram of the bifurcation set (q, γ), showing the paths of limit points (solid curves) and the paths of symmetry-breaking bifurcation points (broken curves) as the aspect ratio varies, for radius of curvature $\beta = 50$.

to 3.7. At $q = 3420$, the magnitude of the negative real part had increased, and this trend continued to $q = 4000$, where the imaginary part was 16.6. We repeated these eigenvalue calculations at the radius of curvature $\beta = 12.9$ used by Hille *et al.*, with similar conclusions.

We conclude from the above calculations that the A_1 branch is genuinely unstable with respect to perturbations that break the horizontal symmetry, in the present approximation of fully developed flow. The existence of a pair of complex eigenvalues of negative real part suggests that it is unstable in an oscillatory fashion for values of q between L_2 and L_3.

3.2. *Rectangular cross-section*

The methods described in §2 were used to follow the paths of limit points and symmetry-breaking bifurcation points found at $\gamma = 1$, as the aspect ratio varied. In this way the bifurcation set in the parameters (q, γ) was obtained, for a fixed value of $\beta = 50$.

3.2.1. *Bifurcation set* (q, γ)

The bifurcation set is complex and a schematic diagram is shown in figure 7. First, we consider the paths of limit points, which are shown as solid lines. The location of the limit points at $\gamma = 1$ is indicated. The minimum value of q for the appearance of multiple solutions, which is determined by the location of L_1, decreases as the aspect ratio increases. In contrast, the limit point L_2, which marks the disappearance of the primary two-cell flow, first moves to smaller q, then to larger q, until it reaches the turning-point T_1, where it merges with the limit point L_3. T_1 is a transcritical bifurcation point, represented schematically in figure 2 (*d*). For aspect ratios greater than T_1, there is only a single limit point L_1 and the branch S_2/S_3 is disconnected

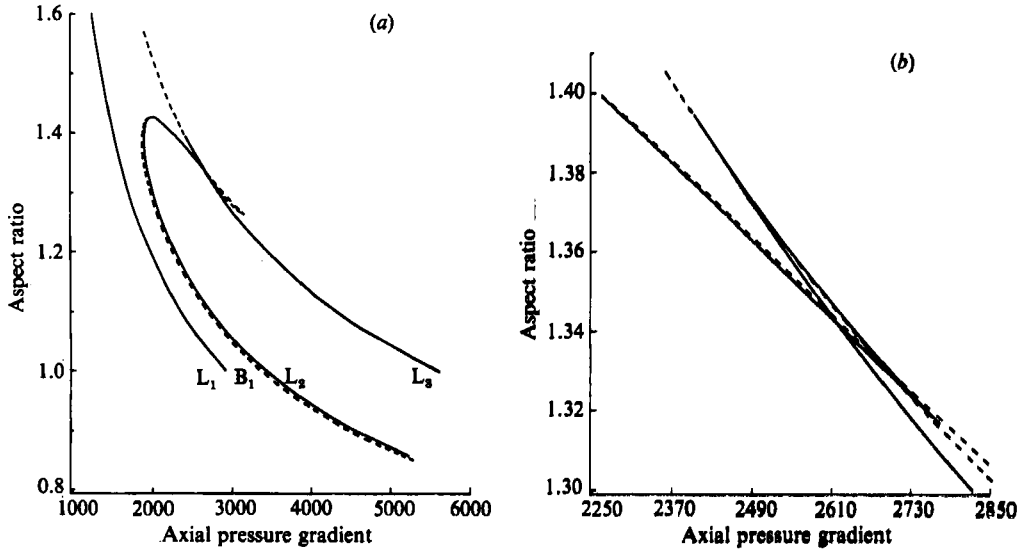

FIGURE 8. (*a*) Computed bifurcation set (q, γ) for a radius of curvature $\beta = 50$, with the same notation as in figure 7. (*b*) Enlargement in the region of the 'swallowtail'.

Singular point	Grid	q	γ	Dn
T_1	32 × 32h	1992.29	1.42566	76.06
	24 × 24h	1992.03	1.42576	76.06
	16 × 16h	1990.18	1.42634	76.03
	12 × 12h	1982.99	1.42806	75.88
C_1	12 × 12h	1978.53	1.42837	75.74
C_2	12 × 12h	3122.24	1.26395	101.0
H_1	24 × 24h	2366.09	1.40342	85.99
	20 × 20h	2367.25	1.40319	86.02
	16 × 16h	2371.48	1.40219	86.12
	12 × 12h	2399.70	1.39486	86.71
H_2	24 × 24h	2773.26	1.31688	94.34
	20 × 20h	2773.59	1.31689	94.35
	16 × 16h	2774.43	1.31682	94.37
	12 × 12h	2774.88	1.31642	94.39
D_1	20 × 20h	2107.32	1.41872	79.35
	16 × 16h	2109.15	1.41879	79.41
	12 × 12h	2112.79	1.41924	79.56
D_2	20 × 20h	2421.40	1.38931	87.22
	16 × 16h	2427.53	1.38792	87.35
	12 × 12h	2468.47	1.37797	88.21
Q_1	12 × 12h	3082.80	1.26838	100.2
Q_2	12 × 12h	2992.08	1.28454	98.69

TABLE 2. Singular points of codimension 2, at $\beta = 50$: T, transcritical point; C, coalescence point; H, non-degenerate hysteresis point; D, double-singular point; Q, quartic point

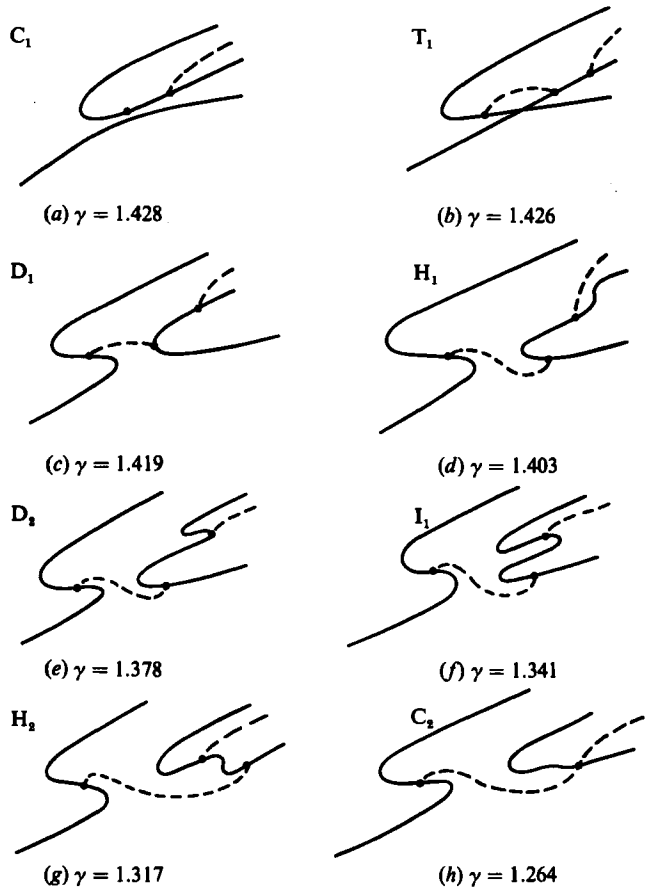

FIGURE 9. Schematic state diagrams showing the variation of a measure of the symmetric component of the solution χ_s with the axial pressure gradient q, for aspect ratios between 1.264 and 1.428. A broken line indicates an asymmetric solution.

from the primary two-cell branch S_1. The limit point L_3, which marks the reappearance of the two-cell flow, traces out a complex path which crosses over itself and forms a pair of non-degenerate hysteresis points H_1 and H_2. This structure is typical of an unfolded swallowtail catastrophe, but it is not clear what the unfolding parameter is in this case; we shall see later that it is not the radius of curvature β. The 'swallowtail' corresponds to the creation and collapse of additional pairs of limit points on the S_4 and S_5 branches.

The path of the symmetry-breaking bifurcation point B_1, which is traced out by varying the aspect ratio, is also complex. It has two turning-points C_1 and C_2, which are coalescence points, two double-singular points D_1 and D_2 where it touches a path of limit points, and two quartic points Q_1 and Q_2 where the type of bifurcation changes between supercritical and subcritical.

It should be noted that the crossing of the paths of symmetry-breaking bifurcation points is possible because they lie on different branches, having looped around the non-degenerate hysteresis point H_2.

The schematic diagram of figure 7 is incomplete in that we have not calculated the paths of limit points that arise at Q_1 and Q_2. Similarly, we have not computed the

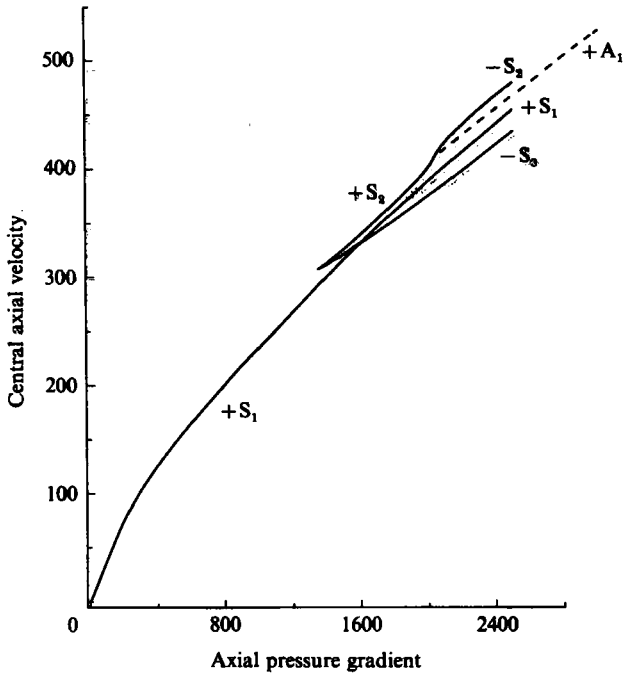

FIGURE 10. Computed state diagram showing the variation of central axial velocity with q, for an aspect ratio $\gamma = 1.5$ and a radius of curvature $\beta = 50$.

paths of Hopf bifurcation points that are known to arise at double-singular points such as D_1 and D_2. It is now apparent that the limit points L_4 and L_5 found on the asymmetric branch A_1 at $\gamma = 1$ have their origin at the quartic points Q_1 and Q_2.

The actual bifurcation set is shown in figure 8(*a*) with an enlargement of the 'swallowtail' in figure 8(*b*). The transcritical bifurcation point is located at $\gamma = 1.426$, so that for aspect ratios greater than this value the two-cell flow branch is continuous at all q, and the four-cell branch is completely disconnected. It is apparent from figure 8(*b*) that the swallowtail effect is confined to a narrow range of aspect ratios, from 1.32 to 1.40. The symmetry-breaking bifurcation points lie very close to the limit points L_2 and L_3. The locations of the singular points in figure 8 are given in table 2 for different grids.

3.2.2. *Solution structure*

For aspect ratios greater than 1.426 the state diagram has the simple structure shown schematically in figure 9(*a*). However, a more complex form develops for values of γ in the range in which the higher-order singularities of the bifurcation set appear. Figure 9 shows the state diagrams schematically, at each of the singular points on figure 7, in decreasing order of aspect ratio. An additional point I_1 is included, which corresponds to the intersection of the paths of limit points, although this is not a singular point. This sequence of state diagrams shows the complex manner in which the unfolded transcritical bifurcation of the square cross-section develops from the disconnected structure seen for γ greater than 1.426.

The actual solution structure for an aspect ratio of 1.5 is shown in figure 10. As in figure 4, the central axial velocity is used as a measure of the symmetric component

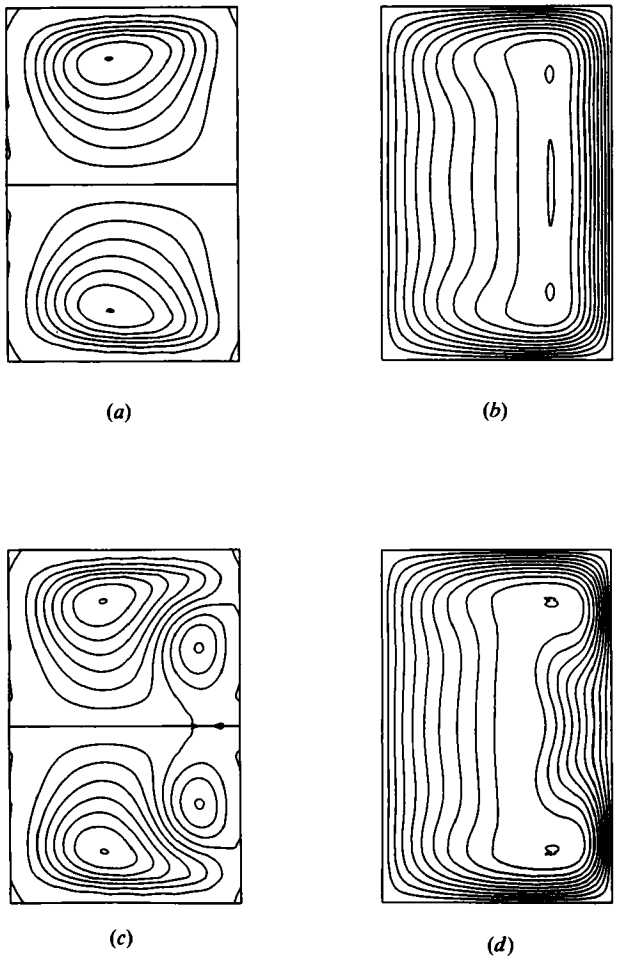

FIGURE 11*a–d*. For caption see facing page.

of the solution. However, with this measure the S_3 branch now lies *below* the S_2 branch, in contrast to the $\gamma = 1$ case. As we have discussed, the primary two-cell flow is disconnected from the secondary four-cell branch. The effect of the asymmetric branch arising from the symmetry-breaking bifurcation point is to destabilize the S_3 branch, as for the square cross-section. Thus, all solutions except the primary two-cell flow are predicted to be unstable. The stability of the branches was verified by explicit computation of the lowest eigenvalues of the Jacobian matrix, as for the square cross-section. For $\gamma = 1.5$, there is clearly no range of axial pressure gradient over which there are no two-cell flows.

The contours of stream function and axial velocity at $q = 2500$ are shown in figure 11. The asymmetry of the flow on the A_1 branch is particularly pronounced, and the additional vortices of the four-cell flow are very strong.

3.3. *Effect of radius of curvature*

The final part of the present study concerns the effect of the radius of curvature on the location of the singular points. The aim is to obtain some indication of the validity

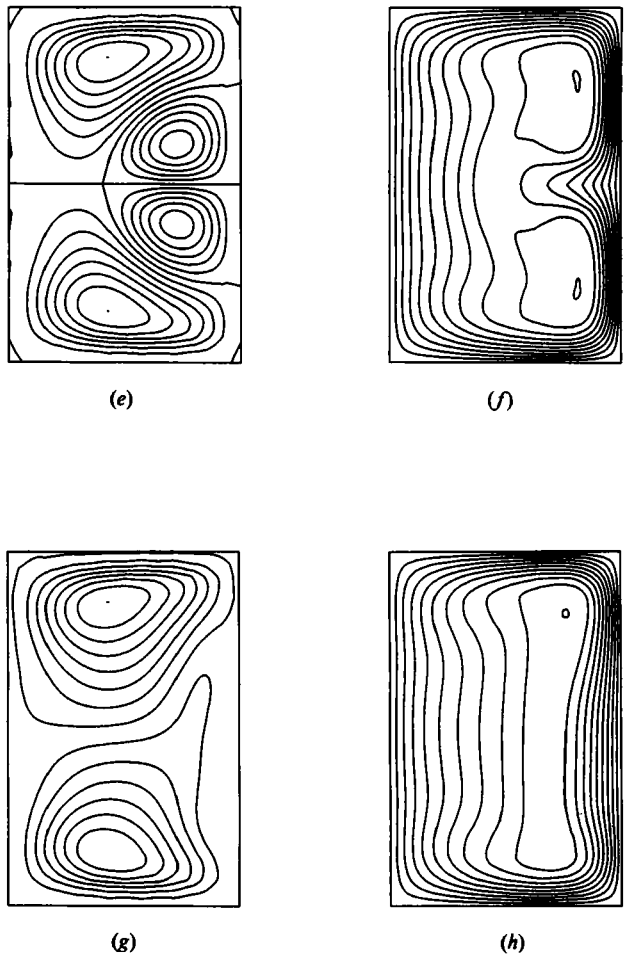

FIGURE 11. Multiple solutions for $\gamma = 1.5$ at an axial pressure gradient $q = 2500$ and radius of curvature $\beta = 50$. (*a*) Streamlines and (*b*) axial velocity contours on the branch S_1; (*c*) streamlines and (*d*) axial velocity contours on the branch S_2; (*e*) streamlines and (*f*) axial velocity contours on the branch S_3; (*g*) streamlines and (*h*) axial velocity contours on the branch A_1.

of the assumption that the Dean number characterizes the flow, and to allow a more meaningful comparison with other work which has been performed at various curvature ratios.

Figure 12(*a*) shows the variation in the values of axial gradient q for the singular points L_1, L_2, L_3 and B_1 at $\gamma = 1$, and the higher-order singularities T_1, H_1 and H_2. Their location moves to increasingly smaller q as the radius of curvature is decreased. Figure 12(*b*) shows the variation in the derived values of the Dean number Dn for the same singular points. There is comparatively little variation in the critical Dean numbers for large values of β, but the singular points move to increasingly higher values of Dn as the radius of curvature is decreased below 20. The variation when β exceeds 50 is small and is not shown. As an example, L_1 varies between $Dn = 79.1$ at $\beta = 200$ and $Dn = 80.3$ at $\beta = 50$.

The experiments of Hille *et al.* (1985) used a radius of curvature of 12.9, and it is

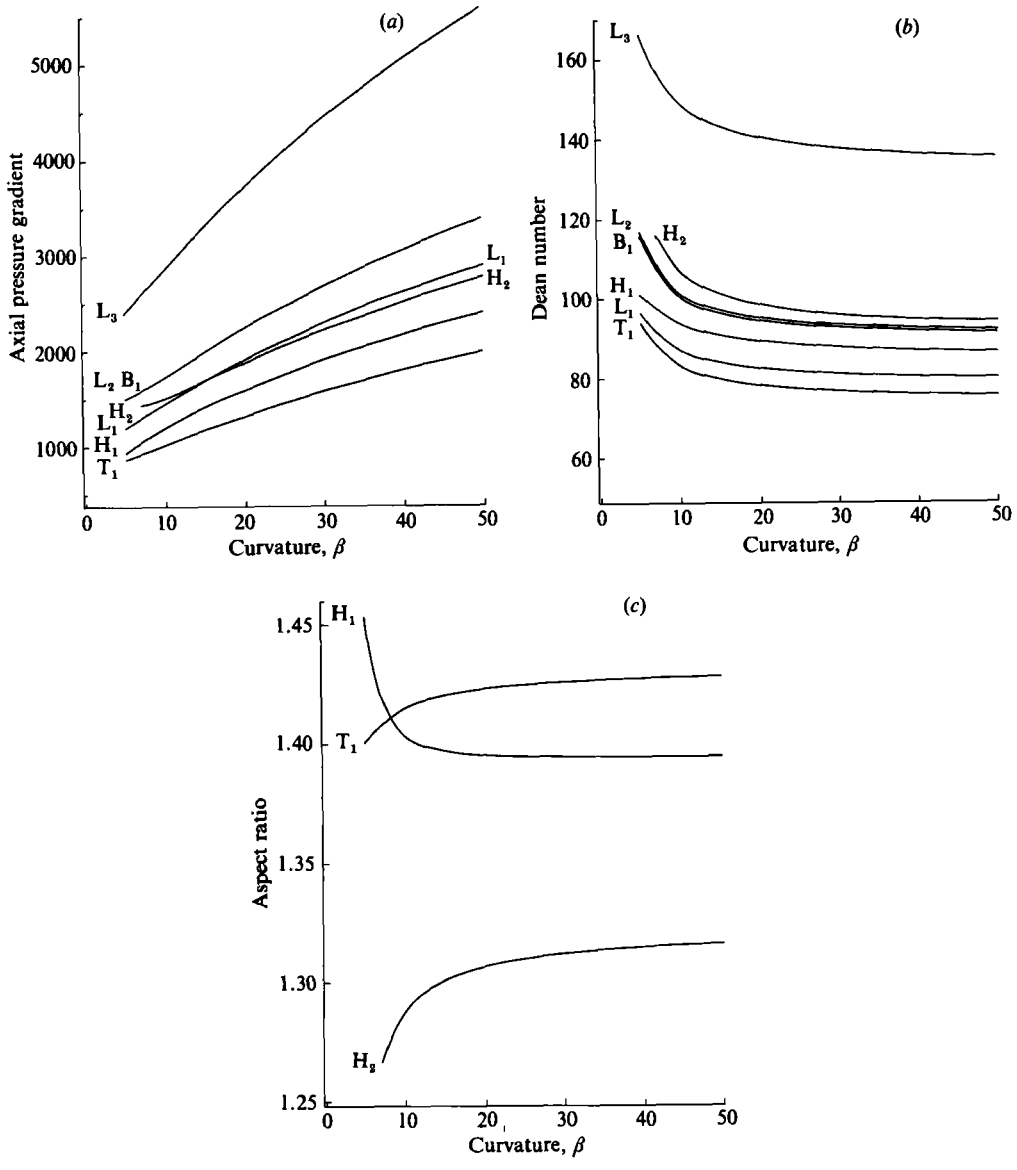

FIGURE 12. The effect of radius of curvature on (*a*) axial pressure gradient, (*b*) Dean number, (*c*) aspect ratio, for the singular points indicated.

interesting that there is strong variation in the location of the singular points at this value of β. The critical Dean number corresponding to L_2 is 98.5, which is closer to the value of 106 for the observed transition from two- to four-cell flow.

Figure 12(*c*) shows the variation in the critical aspect ratio γ for the higher-order singularities T_1, H_1 and H_2. The separation in aspect ratio of the two non-degenerate hysteresis points actually increases as the curvature ratio is reduced, and is constant at large β, so that β is not the unfolding parameter for the 'swallowtail'.

These results show that there is only a small variation in the derived Dean number for curvatures above 20, but below this value Dn is increasingly sensitive to β.

However, it is important to note that the relationship between the singular points remains constant, even at small β, and so the bifurcation set (Dn, γ) remains qualitatively the same.

4. Conclusions

A detailed study of fully developed, laminar flow within a curved tube of rectangular cross-section has been presented. The solution structure was resolved using extended systems based on the Navier–Stokes equations to locate exactly the critical values of axial pressure gradient for a square cross-section. Continuation methods were used to trace the paths of the singular points as the aspect ratio and radius of curvature varied.

In the case of a square cross-section, the structure of the symmetric solutions was found to be an unfolded transcritical bifurcation, with multiple symmetric solutions in two distinct ranges of axial pressure gradient q. In addition, a symmetry-breaking bifurcation point was found to give rise to a pair of asymmetric solutions above a critical value of q. The predicted structure clarifies the nature of the transition from two- to four-cell flow reported in previous work.

Continuation of the solutions to different aspect ratios reveals a complex bifurcation set in the parameters q and γ, with a number of higher-order singularities. In particular the path of limit points crosses in the manner of an unfolded swallowtail catastrophe. The transcritical bifurcation point was found to be located at $\gamma = 1.43$; for higher aspect ratios the secondary four-cell branch is disconnected from that of the primary solution.

The stability of the solutions was analysed and it was found that, in the present approximation of fully developed flow, all multiple solutions except the two-cell type are unstable with respect to either symmetric or antisymmetric perturbations. For values of the aspect ratio less than 1.43 there is a region of Dean numbers for which there is no stable flow. The unstable, asymmetric flows in this region are similar to those observed in the experiments of Hille *et al.* (1985).

We have demonstrated the importance of the asymmetric solutions in determining the stability of the symmetric flows in a curved tube. This highlights the danger of imposing the symmetry of the flow equations onto the solution itself; such an assumption excludes the possibility of asymmetric flows, and in general it may lead to the prediction of an incomplete solution structure with incorrect stability properties.

The effect of radius of curvature was also investigated. The critical Dean numbers of the singular points were found to vary strongly at small values of the radius of curvature, but the bifurcation set remained qualitatively the same.

We have shown that the complex structure arising from the nonlinear equations is revealed in an efficient way by using extended systems with parameter continuation. It is intended to use this approach to identify the nature of the dual solutions found for other cross-sections.

It is a pleasure to thank K. A. Cliffe for many discussions, and Drs T. Mullin and M. J. Norgett for helpful comments.

REFERENCES

BENJAMIN, T. B. 1978 Bifurcation phenomena in steady flows of a viscous fluid. *Proc. R. Soc. Lond.* A **59**, 1–26.

CHENG, K. C., LIN, R.-C. & OU, J.-W. 1976 Fully-developed laminar flow in curved rectangular channels. *Trans. ASME* I: *J. Fluids Engng* **98**, 41–48.

CLIFFE, K. A. 1983 Numerical calculations of two-cell and single-cell Taylor flows. *J. Fluid Mech.* **135**, 219–233.

CLIFFE, K. A. 1984 Numerical calculations of the primary flow exchange process in the Taylor Problem. *Harwell Rep.* AERE TP.1060.

CLIFFE, K. A. & MULLIN, T. 1985 A numerical and experimental study of anomalous modes in the Taylor experiment. *J. Fluid Mech.* **153**, 243–258.

CLIFFE, K. A. & SPENCE, A. 1984 The calculation of high order singularities in the finite Taylor problem. In *Numerical Methods for Bifurcation Problems* (ed. T. Küpper, H. D. Mittleman & H. Weber). Birkhäuser: ISNM.

CLIFFE, K. A. & WINTERS, K. H. 1983 The Moore algorithm for bifurcation point location: its application to natural convection using the finite element code TGSL. *Harwell Rep.* AERE M.3352.

CLIFFE, K. A. & WINTERS, K. H. 1984 A numerical study of the cusp catastrophe for Bénard convection in tilted cavities. *J. Comp. Phys.* **54**, 531–534.

CLIFFE, K. A. & WINTERS, K. H. 1986 The use of symmetry in bifurcation calculations and its application to the Bénard problem. *J. Comp. Phys.* **67**, 310–326.

DEAN, W. R. 1928 The stream-line motion of fluid in a curved pipe. *Phil. Mag.* **5**, 673–695.

DENNIS, S. C. R. & NG, M. 1982 Dual solutions for steady laminar flow through a curved tube. *Q. J. Mech. Appl. Math.* **35**, 305–324.

DE VRIEND, H. J. 1981 Velocity redistribution in curved rectangular channels. *J. Fluid Mech.* **107**, 423–439.

GHIA, K. N. & SOKHEY, J. S. 1977 Laminar incompressible viscous flow in curved ducts of regular cross-section. *Trans. ASME* I: *J. Fluids Engng* **99**, 640–648.

HILLE, P., VEHRENKAMP, R. & SCHULZ-DUBOIS, E. O. 1985 The development and structure of primary and secondary flow in a curved square duct. *J. Fluid Mech.* **151**, 219–241.

KELLER, H. B. 1977 Numerical solutions of bifurcation and nonlinear eigenvalue problems. In *Applications of Bifurcation Theory* (ed. P. H. Rabinowitz), pp. 359–384. Academic.

JACKSON, C. P. & WINTERS, K. H. 1984 A finite-element study of the Bénard problem using parameter-stepping and bifurcation search. *Intl J. Num. Meth. Fluids* **4**, 127–145.

JEPSON, A. & SPENCE, A. 1984 Singular points and their computation. In *Numerical Methods for Bifurcation Problems* (ed. T. Küpper, H. D. Mittleman & H. Weber). Birkhäuser: ISNM.

JEPSON, A. & SPENCE, A. 1985 Folds in solutions of two parameter systems and their calculation. Part I. *SIAM J. Numer. Anal.* **22**, 736–759.

JOSEPH, B., SMITH, E. P. & ADLER, R. J. 1975 Numerical treatment of laminar flow in helically coiled tubes of square cross-section. *AIChE J.* **21**, 965–974.

MANLAPAZ, R. L. & CHURCHILL, S. W. 1980 Fully developed laminar flow in a helically coiled tube of finite pitch. *Chem. Engng Commun.* **7**, 57–78.

MASLIYAH, J. H. 1980 On laminar flow in curved semicircular ducts. *J. Fluid Mech.* **99**, 469–479.

MOORE, G. & SPENCE, A. 1980 The calculation of turning points of non-linear equations. *SIAM J. Numer. Anal.* **17**, 567–576.

NANDAKUMAR, K. & MASLIYAH, J. H. 1982 Bifurcation in steady laminar flow through curved tubes. *J. Fluid Mech.* **119**, 475–490.

ROOSE, D. & CALUWAERTS, R. 1984 Direct methods for the computation of a nonsimple turning point corresponding to a cusp. In *Numerical Methods for Bifurcation Problems* (ed. T. Küpper, H. D. Mittleman & H. Weber). Birkhäuser: ISNM.

SPENCE, A. & JEPSON, A. 1984 The numerical calculation of cusps, bifurcation points and isola formation points in two parameter problems. In *Numerical Methods for Bifurcation Problems* (ed. T. Küpper, H. D. Mittleman & H. Weber). Birkhäuser: ISNM.

THOMSON, J. 1876 On the origin of windings of rivers in alluvial plains, with remarks on the flow of water round bends in pipes. *Proc. R. Soc. Lond.* A **25**, 5–8.

WERNER, B. 1984 Regular systems for bifurcation points with underlying symmetries. In *Numerical Methods for Bifurcation Problems* (ed. T. Küpper, H. D. Mittleman & H. Weber). Birkhäuser: ISNM.

WERNER, B. & SPENCE, A. 1984 The computation of symmetry-breaking bifurcation points. *SIAM J. Numer. Anal.* **21**, 388–399.

WINTERS, K. H. & BRINDLEY, R. C. G. 1984 Multiple solutions for laminar flow in helically-coiled tubes. *Harwell Rep.* AERE R.11373.

WINTERS, K. H. & CLIFFE, K. A. 1985 Convergence properties of the finite-element method for Bénard convection in an infinite layer. *J. Comp. Phys.* **60**, 346–351.

WINTERS, K. H., CLIFFE, K. A. & JACKSON, C. P. 1984 A review of extended systems for finding critical points in coupled problems. In *Numerical Methods for Transient and Coupled Problems* (ed. R. W. Lewis, E. Hinton, P. Bettess and B. A. Schrefler). Swansea: Pineridge.